

Competing structural instabilities in Bi_2SiO_5

A. Girard,^{1,*} H. Taniguchi,² S. M. Souliou,³ M. Stekiel,¹ W. Morgenroth,¹ A. Minelli,³
A. Kuwabara,⁴ A. Bosak,³ and B. Winkler¹

¹*Institut für Geowissenschaften, Goethe Universität Frankfurt, Altenhöferallee 1, D-60438 Frankfurt am Main, Germany*

²*Department of Physics, Nagoya University, Nagoya 464-8602, Japan*

³*ESRF - The European Synchrotron, 71, Avenue des Martyrs, F-38000 Grenoble, France*

⁴*Nanostructures Research Laboratory, Japan Fine Ceramics Center, Nagoya 456-8587, Japan*



(Received 31 July 2018; published 9 October 2018)

The lattice dynamics of Bi_2SiO_5 has been studied by x-ray thermal diffuse scattering (TDS), inelastic x-ray scattering (IXS), and density functional theory calculations across the ferroelectric transition at $T_C = 663$ K. Rodlike diffuse features are observed along the [100] direction, perpendicular to the direction of the quasi-one-dimensional silicate chains. IXS measurements of the phonon dispersion along the [100] Γ - Y direction related these diffuse features to coupled unstable transverse optic and acoustic branches. A strong temperature-dependent TDS signal was also observed at the Brillouin zone edges, at the Y and S points, indicating a competition between ferroelectric and antiferroelectric distortions. We observed with IXS a substantial but finite phonon softening at the Y point and a minor softening at the S point, that are associated with the displacement of oxygen atoms. The good agreement between the experiment and the theoretical TDS and IXS allows us to provide a quantitative overview of the various lattice dynamical instabilities occurring at T_C . The direct evidence for competing ferroelectric and antiferroelectric orders opens the way towards tuning the properties of Bi_2SiO_5 by application of pressure or electrical field.

DOI: [10.1103/PhysRevB.98.134102](https://doi.org/10.1103/PhysRevB.98.134102)

I. INTRODUCTION

Bi_2SiO_5 (BSO) recently emerged as a promising ambient temperature lead-free ferroelectric (FE) with a Curie temperature $T_C = 663$ K, where the ferroelectricity arises from the tilt of the quasi-one-dimensional (1D) chains formed by SiO_4 tetrahedral units [1,2]. BSO thus provides an alternative to perovskite-type FE such as in PbTiO_3 [3], BiFeO_3 [4], or BiMnO_3 [5], where the ferroelectricity arises from the cation off-centering. The finding of ferroelectricity driven by 1D silicate chains in BSO opened the route towards the engineering of new tetrahedra-based FE.

The layered monoclinic crystal structure of FE BSO is depicted in Fig. 1. It is composed of $[\text{Bi}_2\text{O}_2]^{2-}$ layers and corner-sharing SiO_4 tetrahedral chains. The Bi_2O_2 layer is formed by BiO_4 square pyramids arranged in a two-dimensional (2D) checkerboard network of pyramids pointing alternatively up and down. The origin of the ferroelectricity in BSO, first evidenced with polarization loop [1] and piezoresponse force microscopy [6] measurements, has been recently studied based on its electron charge density [7] and *ab initio* calculations [8]. The spontaneous polarization was attributed to the large electric dipole moment in the SiO_4 tetrahedra which align in the FE configuration, while the Bi_2O_2 layers align in the antiferroelectric (AFE) configuration with a weak resulting polarization. The FE soft mode, which drives the transition at T_C , corresponds to a torsion of the SiO_4 units along the 1D tetrahedral chains. The dynamics of the soft

mode across the transition at T_C has been previously reported at the Γ point using Raman spectroscopy [1], where the power-law dependence of the phonon softening was observed according to the prediction of Cochran's law [9]. However, the *ab initio* calculations of the phonon dispersion reported by Taniguchi *et al.* [1] for the high-temperature $Cmcm$ phase also predicted imaginary phonon energies at the Y and S points, in addition to the Γ instability. Usually, instabilities at the Brillouin zone edges are related to AFE ordering through the condensation of an AFE optical soft mode [10–12]. While density functional theory (DFT)-based calculations of phonon dispersion curves are generally reliable [13–18], they are mostly limited to the athermal limit and the harmonic approximation. Therefore, the understanding of the lattice dynamics of BSO away from the Γ point remains incomplete and needs to be studied at the S and Y points in order to obtain a comprehensive picture of the competition between the FE and AFE instabilities.

We report a study of the lattice dynamics of BSO using combined temperature-dependent x-ray thermal diffuse scattering (TDS) and inelastic x-ray scattering (IXS). The IXS and TDS results are compared to the theoretical IXS spectra and TDS maps calculated *ab initio* in the harmonic approximation. Together, these results provide a comprehensive picture of the lattice dynamics of BSO and allow discussing the competition between the different structural instabilities occurring at the Y , S , and Γ points.

II. METHODS

Bi_2O_3 and SiO_2 powders were mixed in an agate mortar in a stoichiometric ratio and heated in a Pt crucible at 1373 K

*Corresponding author: adrien.girard@sorbonne-universite.fr

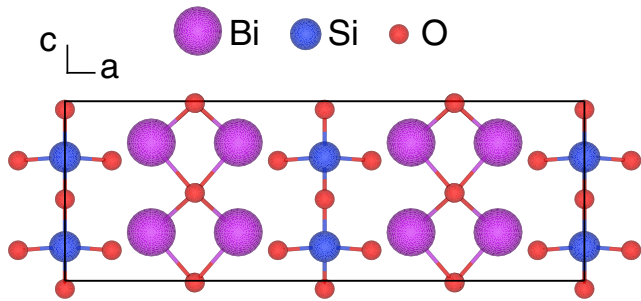


FIG. 1. The crystal structure of Bi_2SiO_5 in the ferroelectric phase. The SiO_4 chains are oriented along the c axis.

over 2 h. The resulting melt was subsequently cooled to ambient temperature, yielding BSO single crystals as thin plates with [100] as the plate normal. The diffuse scattering (DS) experiments were carried out on the side station of the ID28 beamline of the European Synchrotron Radiation Facility (ESRF). We used a monochromatic beam with an energy of 12.6 keV. The reciprocal space maps were acquired with a Pilatus $3 \times 1\text{M}$ detector for several temperatures between room temperature (RT) and 820 K. The sample temperature was controlled with a heat-blower system with an accuracy of ± 5 K. The IXS experiments were then performed at the ID28 beamline of the ESRF, using the high-resolution spectrometer operated at an energy of 17.9 keV, offering an energy resolution of 3 meV. For the temperature-dependent IXS experiment, the temperature was controlled with the same heat blower as for the diffuse scattering experiment.

First-principles calculations were carried out within the framework of DFT [19] and the pseudopotential method using the CASTEP [20] simulation package. “On the fly” norm-conserving pseudopotentials from the CASTEP database were employed in conjunction with plane waves up to a kinetic energy cutoff of 800 eV. A Monkhorst-Pack [21] grid was used for Brillouin-zone integrations with a distance of $< 0.023 \text{ \AA}^{-1}$ between grid points. Convergence criteria included an energy change of $< 5 \times 10^{-6}$ eV/atom for self-consistent-field (SCF)

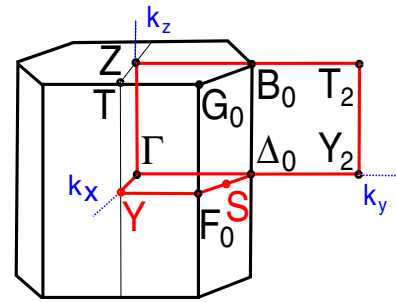


FIG. 2. The Brillouin zone of the BSO paraelectric Cmc structure, showing the Y and S points (in red) where instable phonons modes lead to imaginary frequencies [1].

cycles, a maximal force of $< 0.008 \text{ eV/\AA}$, and a maximal component of the stress tensor < 0.02 GPa. Phonon frequencies were obtained from density functional perturbation theory (DFPT) calculations.

The IXS and TDS intensities were calculated in the first-order and one-phonon approximation. The phonon energies and polarization vectors were obtained from the DFPT phonon calculations. The sensitivity of the TDS to low-energy phonons is due to the strong energy dependence of the TDS intensity, which is

$$I_{\text{TDS}}(\mathbf{Q}) \sim [1/\omega(\mathbf{q})] \coth[\hbar\omega(\mathbf{q})/2k_{\text{B}}T] f(\mathbf{Q})^2, \quad (1)$$

where \mathbf{Q} represents the momentum transfer, \mathbf{q} the reduced momentum transfer, ω the frequency of the phonon, $f(\mathbf{Q})$ the atomic scattering factor, \hbar the reduced Planck constant, k_{B} the Boltzmann constant, and T the temperature.

III. RESULTS

Previous calculated phonon dispersion relations of BSO showed anomalies in the paraelectric Cmc phase at the Y , S , and Γ points [1]. In the FE phase for which there is some uncertainty about the space group ($Cmc2_1$ or Cc , see below and the discussion of the theoretical results), these points have different coordinates. The monoclinic distortion,

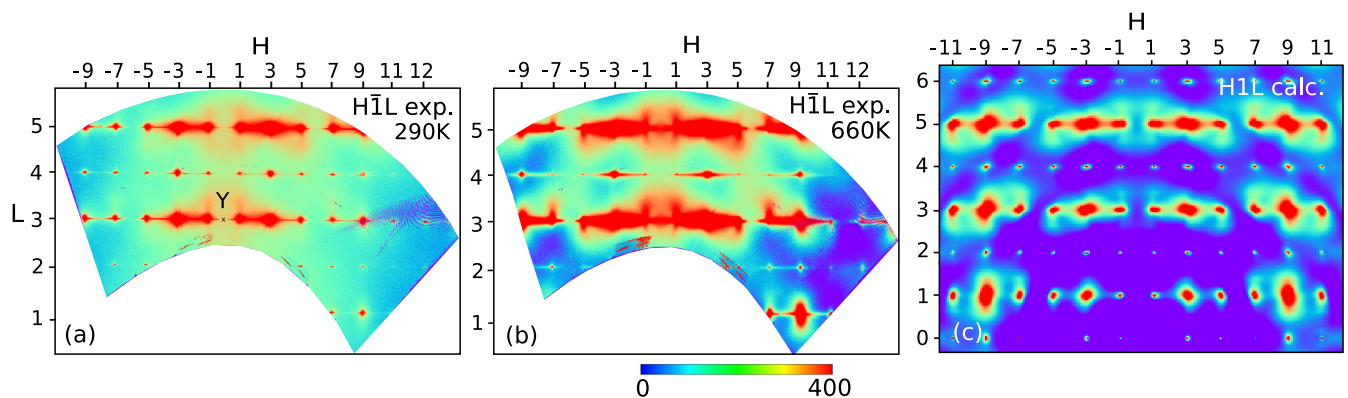


FIG. 3. Reconstructed TDS maps for the FE phase in the $H\bar{L}$ plane measured (a) at RT conditions, (b) close to T_C at $T = 660$ K, and (c) calculated from DFT. The calculated intensities were rescaled to the experimental ones for display purposes. The Y point is indicated and shows a strong temperature dependence due to the incomplete softening of the AFE soft mode close to the FE transition. The rodlike TDS objects due to the soft transverse acoustic (TA) and transverse optic (TO) phonon branches along the Γ - Y direction are already present at RT.

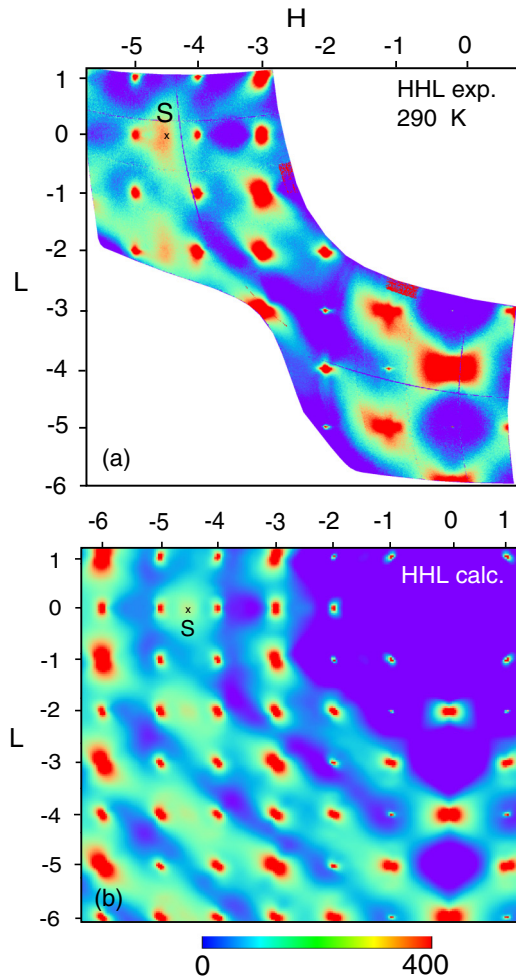


FIG. 4. (a) Experimental ($T = 290$ K) and (b) calculated TDS maps in the HHL plane for FE phase. The calculated intensities were rescaled to the experimental ones for display purposes. The S point is indicated, where a maximum of scattered intensity is observed due to a low-energy optical phonon.

which was inferred from electron diffraction [1], is very small and less than the uncertainties of either diffraction measurements or DFT calculations. It is therefore difficult to ascertain whether the space group of the FE phase is monoclinic or orthorhombic. For consistency, we will keep using in the low-temperature FE phase the notations of the high-temperature paraelectric $Cmcm$ space group, where the Y and S points have coordinates $(1,0,0)$ and $(1/2, 1/2, 0)$, respectively. A schematic view of the Brillouin zone of the $Cmcm$ space group is displayed in Fig. 2, where the Y and S points are highlighted in red color. The DFT calculations carried out in this study for the FE phase lead to the following lattice parameters in the $Cmc2_1$ setting, $a_{Cmc2_1} = 15.456$ Å, $b_{Cmc2_1} = 5.563$ Å, $c_{Cmc2_1} = 5.420$ Å, and agree with the experimental ones within 2%. In the Cc setting they are $a_{Cc} = 15.577$ Å, $b_{Cc} = 5.623$ Å, $c_{Cc} = 5.474$ Å, $\beta = 90.002^\circ$, and agree with the experimental ones within 4%. In the following, the phonon calculations were carried out in the Cc settings.

We started our investigation with a DS survey in order to pinpoint the regions of interest in reciprocal space. The ex-

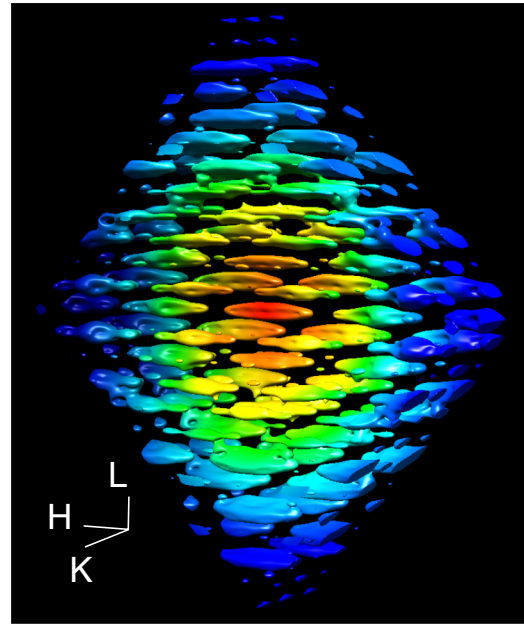


FIG. 5. Theoretical 3D TDS intensity distribution showing the highly anisotropic rodlike intensity distribution. The red spot at the center corresponds to the 002 Bragg reflection.

perimental reconstructed reciprocal space maps measured at RT in the $H\bar{1}L$ and HHL planes are shown in Figs. 3(a) and 4(a), respectively. They show complex and highly anisotropic diffuse features. In the $H\bar{1}L$ plane, we observed at ambient conditions elongated rodlike objects oriented along the $[100]$ direction. These diffuse features occur together with sharper streaks, also oriented along H , due to 2D defects perpendicular to the silicate quasi-1D chains oriented along c . In the HHL plane, the DS intensity distribution is also anisotropic. In the vicinity of the strong Bragg reflections, where the DS is dominated by the contribution of the acoustic phonons, we observed diffuse patterns with a butterfly shape. At small reduced momentum transfers q , the diffuse intensity due to the acoustic phonons scales as $I_{TDS} \sim 1/\omega^2$, where ω is the acoustic phonon frequency. These patterns thus originate from the elastic anisotropy.

Here, we are interested in the lattice dynamics at the S and Y points, which are highlighted in Figs. 4(a) and 3(a) at the positions $(4.5, 4.5, 0)$ and $(0, \bar{1}, 3)$, respectively. A maximum of DS intensity is observed at RT at the S point while no particular DS feature was observed at the Y point. In order to clarify the origin of the observed DS signal at the S point, we calculated the corresponding HHL TDS map, which is compared to the experiment in Fig. 4(b). For the calculated $H\bar{1}L$ plane, see Fig. 3(c). We note an excellent agreement, indicating that all the observed signal is due to the lattice dynamics. All features are well reproduced by the calculations, including the DS intensity maximum at the S point and the rodlike objects. The theoretical TDS intensity distribution, and especially the diffuse rods, can be better visualized with three-dimensional (3D) reconstruction, shown in Fig. 5, which clearly evidences the anisotropic TDS intensity distribution close to the strong Bragg peaks oriented along the $[100]$ direction.

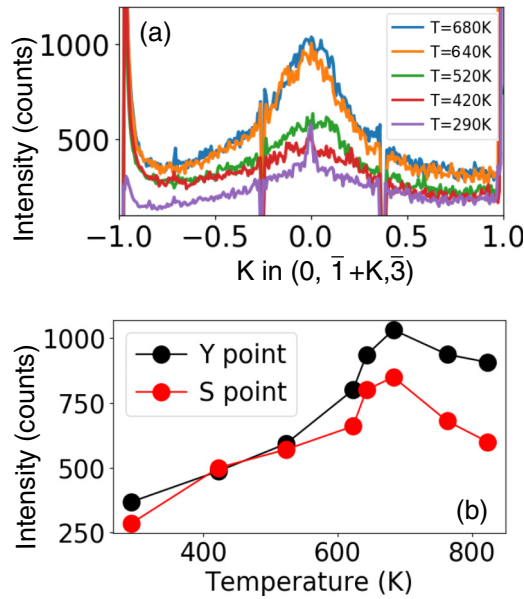


FIG. 6. (a) 1D TDS intensity profiles normalized to the background across the Y point in the $(0, \bar{2} + K, \bar{3})$ direction, showing the strong increase of the TDS signal centered at the Y point upon approaching T_C . (b) Comparison of the temperature dependence of the TDS intensities measured at the Y and S points.

In order to obtain an overview of the evolution of the low-energy lattice dynamics upon approaching the FE phase transition at 663 K, we followed the temperature dependence of the TDS signal from RT up to 820 K. Upon heating, the most striking changes were observed in the $H\bar{1}L$ plane, which are shown in Fig. 3(b) for $T = 660$ K, close to T_C . The rodlike diffuse objects along H become much more pronounced, in particular, close to the Bragg reflections such as $9\bar{1}3$, where the effect was not present at RT. Another important change occurs at the Y point of the $1\bar{1}3$ and $1\bar{1}5$ Brillouin zones, where the TDS intensity was a minimum at RT and becomes a maximum close to T_C . To better visualize these intensity variations, we plot in Fig. 6(a) the corresponding 1D intensity profile for various temperatures across the Y point $(0, \bar{1}, 3)$ along the direction $(0, \bar{2} + K, 3)$, perpendicular to the $H\bar{1}L$ plane. The values of the TDS intensity are reported as a function of the temperature in Fig. 6(b). It clearly shows

that the Y -point TDS intensity passes through a maximum at T_C and decreases back after the transition. This behavior is generally attributed to the softening of a phonon at the transition. The same behavior is observed at the S point, where the intensity is also plotted against the temperature in Fig. 6(b).

As a diffuse scattering experiment is not resolved in energy, it is not possible to disentangle the elastic scattering due to static disorder or defects and inelastic scattering due to phonons. In order to unveil the lattice dynamics underlying these TDS intensity distributions, we performed a temperature-dependent IXS experiment, which provides the energy resolution in addition to the momentum resolution. We aimed at following the evolution of the IXS spectra at the Y and S points with the temperature. To this end we first compare the computed IXS intensity maps (in the Cc phase) along the Γ - Y direction for the $(0, \bar{1}, 3)$ Y point and the Γ - S direction for the $(\bar{4}, \bar{4}, 0)$ Bragg reflection direction. This allows us to disentangle the possible multiphonon contribution within one IXS peak. The resulting intensity maps are shown in Figs. 7(a) and 7(b), respectively. Close to Γ , the IXS spectra are dominated by the contribution of the acoustic phonon, whose intensity progressively vanishes towards the Y and S points. At the Y point, the IXS spectra only contain the contribution of a single optical phonon mode at 9.3 meV. Similarly, the IXS intensity at the S point is dominated by a single phonon mode at 4.8 meV.

The experimental IXS maps along the Γ - S direction are shown in Fig. 7(c) for the Cc structure (at RT) and in Fig. 7(d) for the $Cmcm$ structure ($T = 750$ K). The acoustic branch remains unchanged across the transition, while a small softening by 0.4 meV is observed for the optical phonon at the S point. For the Γ - Y direction, we only acquired the detailed temperature dependence of the Y point, because in this direction of the reciprocal space, the IXS signal was largely dominated by the strong elastic scattering from the 2D defects along H [see Fig. 3(a)] preventing any low-energy measurement close to Γ . A selected set of IXS spectra acquired at the Y point is shown in Fig. 8(a) for the temperatures $T = 345$ K ($T \ll T_C$), $T = 495$ K ($T < T_C$), and $T = 650$ K (close to T_C). The spectra were fitted using a damped harmonic oscillator (DHO) model, and the results of the fit are displayed as solid lines.

We can distinguish two important effects in the IXS spectra upon approaching the transition at T_C : (i) A pronounced

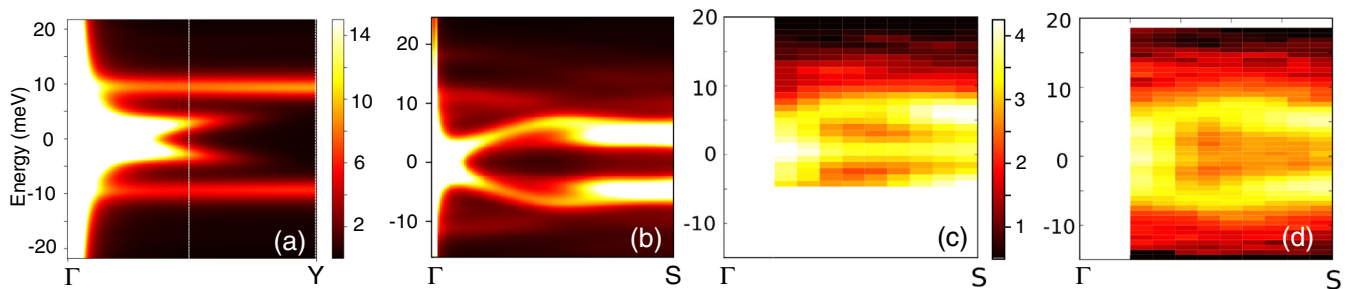


FIG. 7. (a) and (b) Calculated IXS intensity maps of BSO along the Γ - Y and Γ - S directions, respectively (Cc space group). The intensity bar stands for both left-hand-side plots, with black color for zero intensity and white color for high intensities. The vertical dashed line shows the q value where the acoustic phonon was measured (see main text). (c) and (d) IXS intensity maps measured in the FE phase (at RT) and in the paraelectric phase ($T = 800$ K), respectively. The intensity bar stands for both right-hand-side plots.

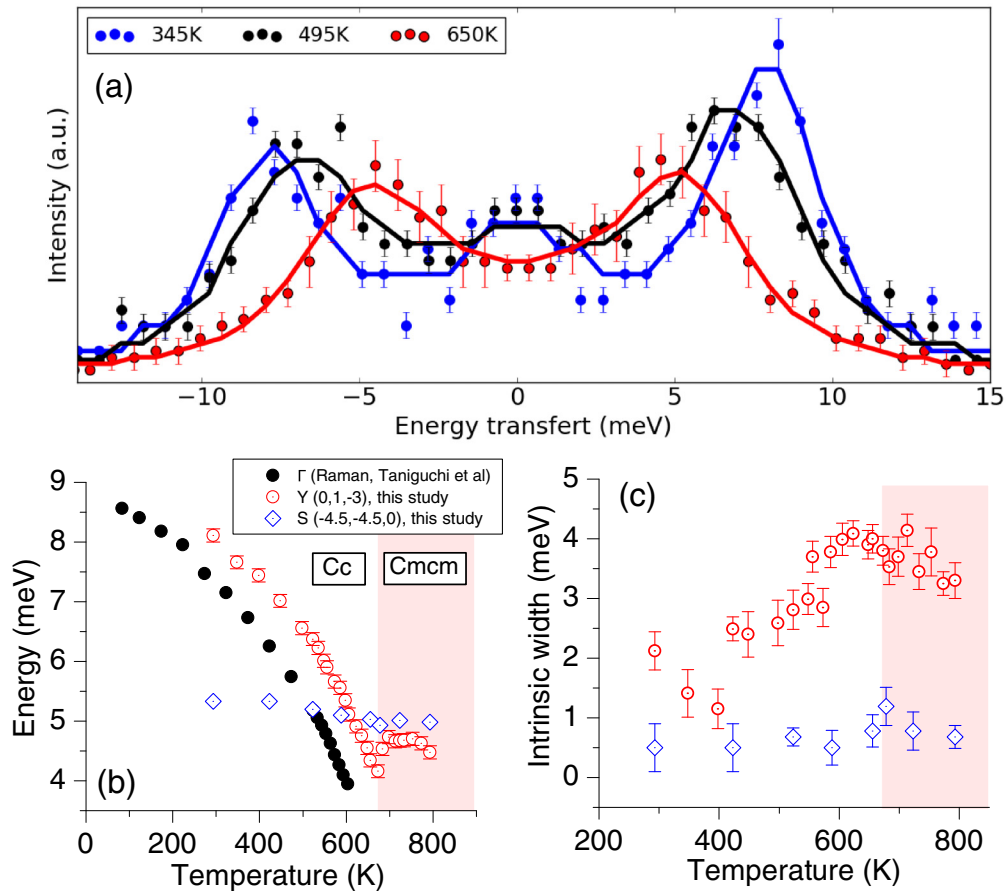


FIG. 8. (a) IXS spectra measured at the Y point for three different temperature: 345 K (blue, $T \ll T_C$), 495 K (black, $T < T_C$), and 650 K (red, $T \sim T_C$). Solid circles are the experimental data with their error bars, and solid lines represent the fit by a DHO model (see text for details). (b) Temperature evolution of the phonon energies at the Y point (red), S point (blue), and Γ point (black). The Γ -point data correspond to the FE soft mode and correspond to the Raman data reported in Ref. [1]. (c) Evolution with temperature of the intrinsic width of the phonon excitations at the Y and S points. The data represent the intrinsic width of the peak fitted by the DHO function and convoluted with the experimental resolution function. The color code is the same as in (b).

softening of the Y point optical phonon is observed. A more detailed evolution of the Y point phonon energy is shown in Fig. 8(b) and compared to that of the Γ optical soft mode. This comparison suggests, together with the energy calculated for the phonon (9.3 meV), that the Y -point phonon has started softening at RT ($E_{RT}^Y = 8.2$ meV). Upon heating, the Y -point phonon undergoes a continuous softening up to T_C where its energy reaches a minimum. The softening is not complete at T_C and the phonon energy remains finite with a decrease of 50% compared to the RT energy. For $T > T_C$, the Y -point phonon suddenly hardens in a small temperature range of 30 K and its energy reaches a maximum of 4.7 meV at 700 K. The S -point softening is also shown in Fig. 8(b), and shows a much smaller temperature dependence. However, its RT energy is much lower than that of the Y -point phonon, which explains the strong TDS signal observed at the S point in the HLL reconstructions (see Fig. 4). The energies of the Y - and S -point phonons cross at about 600 K where the Y -point phonon becomes softer. At T_C , the energy of the S -point phonon has only decreased by 10% and shows no further hardening in the $Cmcm$ phase for $T > T_C$. Interestingly, the energy order of these two modes is reversed in the $Cmcm$ phase compared to that of the Cc

phase, and the Y -point mode has the lowest energy above the transition.

(ii) The second effect is a considerable broadening of the optical phonon near the transition at the Y point which is represented in Fig. 8(c) by the intrinsic width Γ_Y of the fitted DHO excitation. For $T \ll T_C$ the phonon peak is well shaped and not overdamped and at 345 K the fit yielded $\Gamma_Y = 1.4$ meV. Upon approaching T_C , the phonon peak becomes overdamped at the same time as it softens, and the intrinsic width becomes $\Gamma_Y = 4$ meV at the transition. In contrast, the S -point phonon only exhibits minor variations of width across the transition, in agreement with the minor softening observed from the peak position.

Finally, we address the question of the stability of the transverse acoustic (TA) branch along the Γ - Y direction. To this end, we investigated the temperature dependence of the IXS spectra at the point (0.5, $\bar{1}$, 3.05) marked with a vertical dashed line in Fig. 7(a), which contains both the contribution of the soft optical phonon and the TA phonon at lower energy [see the calculated IXS spectra in Fig. 9(a)]. We accepted a small L component in order to be able to measure away from the strong elastic signal caused by the 2D defects, as mentioned above. The RT IXS spectra are in good agreement

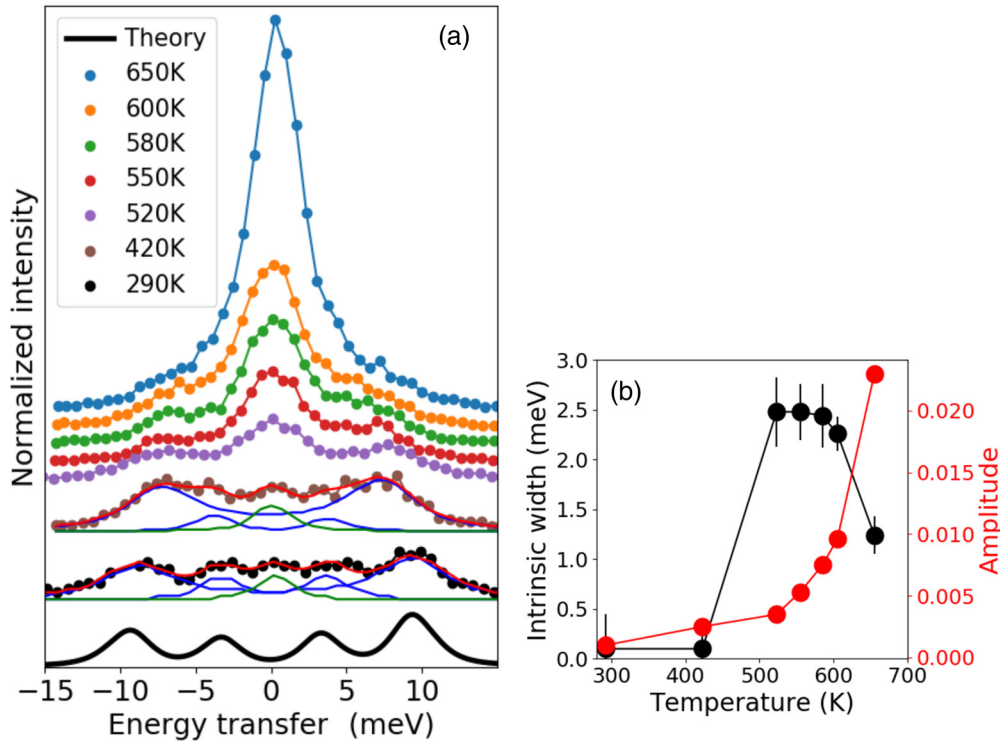


FIG. 9. (A) Evolution with temperature of the IXS spectra measured at $(0.5, \bar{1}, 3.05)$, showing the strong variation of the central peak due to the collapse of the TA branch close to T_C . The TA/TO phonons correspond to the lower-/higher-energy excitations, respectively. Theoretical IXS spectra for the FE phase is shown as a solid black line at the bottom. (b) Evolution with temperature of the intrinsic width (black) and amplitude (red) of the central peak.

with the calculated one (black line), except for the small shift of the optical phonon to lower energies due to the fact that the phonon is already soft at this temperature. The optical phonon shows some moderate softening, in agreement with the Y -point measurements. However, a considerable increase of the central peak intensity is observed upon heating. At 520 K already we cannot distinguish the TA phonon peak from the central line. A closer look at the evolution of the central peak intrinsic width and intensity is shown in Fig. 9(b). The width exhibits a maximum over a 100-K temperature range centered at 550 K, due to the overlap of the phonon line shape with the elastic line. At 650 K, the central line amplitude is even more increased while its width is decreased. This could be due to the softening of the TA phonon, but its small intensity do not allow to draw a conclusion about a possible instability of the TA branch in the high-temperature $Cmcm$ phase.

IV. DISCUSSION

In ferroic materials, the transition at T_C is generally driven by the condensation of the TO polar phonon mode at Γ , whose frequency becomes zero at T_C . In some cases, spectroscopic experiments reported that the TO softening may be observed together with finite wave-vector anomalies in the TA branch. This phenomenon was observed in SrTiO_3 [22,23] and KTaO_3 [24] and various other compounds [25,26]. For SrTiO_3 , it was initially believed that both the transverse zone boundary acoustic mode and the long-wavelength polar soft mode were independent of each other. Later studies showed that it is the polar soft mode that actually drives the structural instability

at $T_S = 105$ K, and that the finite momentum anomaly in the TA branch was due to the strong interaction between the polar soft mode and the acoustic mode through nonlinear electron-lattice coupling [27]. More recently, the interaction between TO and TA modes was rationalized in terms of flexoelectric coupling in the context of AFE PbZrO_3 [28]. The flexoelectric coupling corresponds to a coupling between a strain gradient (the acoustic phonon) with a polarization (the polar optical phonon). This coupling leads to the repulsion between the TO and TA modes and the TO mode softening produces a suppression of the TA frequency [29]. Here, the observed softening of both [100] polarized optical and acoustic phonons in BSO points at a strong TO-TA mode coupling. The anomaly occurs in the Cc phase along the Γ - Y direction, in agreement with the predictions of the DFT calculations of the phonon band dispersion in the high-temperature $Cmcm$ phase [1]. The whole TO phonon branch softens but remains at finite energy, and the repulsion with the acoustic mode produces a collapse of the TA branch. The present energy-resolved IXS data provide a direct evidence for the complete suppression of the TA branch at a single q point $(0.5, \bar{1}, 3)$. However, from the large spatial extent of the TDS intensity variations observed along H in the $H\bar{1}L$ reciprocal space map, we can expect the acoustic collapse to occur over a wider q range along the Γ - Y direction. This dynamical instability in the Cc phase is responsible for the rodlike shape of the diffuse objects shown in Figs. 3 and 5. Interestingly, the overdamping of the Y point phonon [Fig. 8(c)] occurs at 550 K, 120 K before the transition, concomitantly with the onset of the TA branch collapse [red curve, Fig. 9(a)]. This observation is in favor

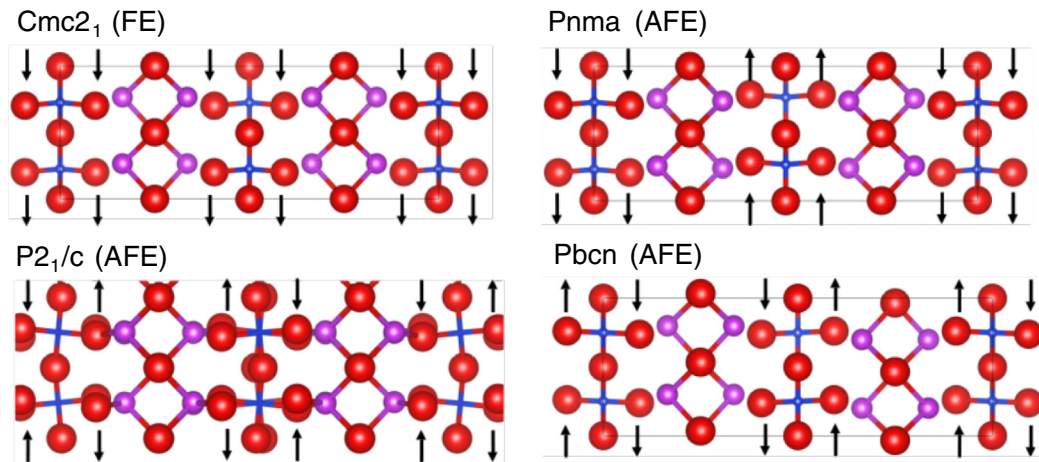


FIG. 10. Structural deformations of $Cmc2_1$, $Pnma$, $P2_1/c$, and $Pbcn$ phases with respect to the $Cmcm$ phase, obtained from the displacement patterns of the corresponding soft modes.

of the scenario of a strong TO-TA mode coupling [30,31], where the interaction between the two phonons produces an increased damping rate of the vibrations.

The simultaneous softening of the soft mode at the Γ and Y points provides a clue to further materials designing based on BSO. Hypothetical structural variations of BSO from the high-temperature $Cmcm$ structure were previously reported; see Supplemental Table 2 in Ref. [1]. Listed in the table are candidates of low-temperature structures, which were obtained by imposing the deformations due to frozen soft modes. According to the energy differences with the $Cmcm$ structure, the most stable structure is the monoclinic Cc , which is obtained by giving an additional shearing to the deformation based on the soft mode at the Γ point. The energy difference between the $Cmc2_1$ and Cc structures is 0.2 meV/f.u., and is contained within the uncertainty of the calculations. This small energy difference reflects the tiny monoclinic distortion discussed above, and it cannot be concluded which of the two phases is the ground state. The next stable structure is the monoclinic $P2c$ structure, which is the result of a the soft mode at the Y point. The present IXS measurements have demonstrated that the energy of the soft mode at the Y point substantially decreases as temperature approaches T_C . Though its softening is incomplete, this behavior suggests that there is an additional instability in BSO due to the Y -point soft mode that competes against the FE instability due to the Γ -point soft mode.

Figure 10 shows the structural deformations of $Cmc2_1$, $Pnma$, $P2_1/c$, and $Pbcn$ phases from the $Cmcm$ phase, which are obtained by the displacement patterns of corresponding soft modes, respectively (see Ref. [1] for calculation details). As presented in the figure, the condensation of the soft mode at the Y point results in the AFE $Pbcn$ structure. The simultaneous softening of the soft modes at the Γ and Y

points thus suggests a competition between the FE and AFE phase transitions in BSO. Judging from the energy difference of 7.8 meV between $Cmc2_1$ and $Pbcn$ structures, it seems possible to tune the ground state of BSO by means of an appropriate perturbation, such as pressure or electric field.

V. CONCLUSION

We performed a detailed study of the lattice dynamics across the FE transition in BSO by means of TDS and IXS measurements and DFT calculations. In addition to the FE instability due to the Γ -point soft mode, our data reveal an AFE instability due to the substantial softening of a TO phonon at the Y point of the Brillouin zone edge. The softening of the Y -point TO phonon branch is possibly accompanied by a suppression of the TA frequency which is presumably driven by TO-TA mode repulsion, indicating a strong TO-TA mode coupling and producing highly anisotropic TDS features. While the FE transition is finally driven by the complete softening of the FE mode at the Γ point, our results provide direct evidence for a strong competition between FE and AFE ordering at T_C . Our work thus opens the route towards the exploration of the boundary between FE and AFE phases of BSO and other similar systems by means of an appropriate external perturbation, such as pressure or electric field.

ACKNOWLEDGMENTS

This study was supported by the BMBF Projects No. 05K13RF1, No. 05K13RF2, No. 05K13RFA, and No. 05K13RFB, and a joint DFG-ANR Project No. WI1232/41-1. We thank Denis Gambetti for technical support in the operation of ID28 beamline of the ESRF. This work is partially supported by a Grant-in-Aid for Young Scientists (A) (No. 16H06115) and MEXT Element Strategy Initiative Project.

[1] H. Taniguchi, A. Kuwabara, J. Kim, Y. Kim, H. Moriwake, S. Kim, T. Hoshiyama, T. Koyama, S. Mori, M. Takata, H.

Hosono, Y. Inaguma, and M. Itoh, *Angew. Chem., Int. Ed.* **52**, 8088 (2013).

- [2] H. Taniguchi, T. Nakane, T. Nagai, C. Moriyoshi, Y. Kuroiwa, A. Kuwabara, M. Mizumaki, K. Nitta, R. Okazaki, and I. Terasaki, *J. Mater. Chem. C* **4**, 3168 (2016).
- [3] G. Shirane, J. D. Axe, J. Harada, and J. P. Remeika, *Phys. Rev. B* **2**, 155 (1970).
- [4] J. B. Neaton, C. Ederer, U. V. Waghmare, N. A. Spaldin, and K. M. Rabe, *Phys. Rev. B* **71**, 014113 (2005).
- [5] R. Seshadri and N. A. Hill, *Chem. Mater.* **13**, 2892 (2001).
- [6] D. Seol, H. Taniguchi, J.-Y. Hwang, M. Itoh, H. Shin, S. W. Kim, and Y. Kim, *Nanoscale* **7**, 11561 (2015).
- [7] Y. Kim, J. Kim, A. Fujiwara, H. Taniguchi, S. Kim, H. Tanaka, K. Sugimoto, K. Kato, M. Itoh, H. Hosono, and M. Takata, *IUCrJ* **1**, 160 (2014).
- [8] J. Park, B. G. Kim, S. Mori, and T. Oguchi, *J. Solid State Chem.* **235**, 68 (2016).
- [9] W. Cochran, *Adv. Phys.* **9**, 387 (1960).
- [10] I. P. Swainson, C. Stock, P. M. Gehring, G. Xu, K. Hirota, Y. Qiu, H. Luo, X. Zhao, J.-F. Li, and D. Viehland, *Phys. Rev. B* **79**, 224301 (2009).
- [11] H. Meister, J. Skalyo, B. C. Frazer, and G. Shirane, *Phys. Rev.* **184**, 550 (1969).
- [12] G. A. Samara, *Phys. Rev. B* **1**, 3777 (1970).
- [13] T. Nguyen-Thanh, A. Bosak, J. D. Bauer, R. Luchitskaia, K. Refson, V. Milman, and B. Winkler, *J. Appl. Crystallogr.* **49**, 1982 (2016).
- [14] M. He, B. Winkler, J. D. Bauer, L. Bayarjargal, J. Ruiz-Fuertes, I. Alencar, W. Morgenroth, K. Refson, and V. Milman, *J. Alloys Compd.* **699**, 16 (2017).
- [15] B. Wehinger, A. Bosak, S. Nazzareni, D. Antonangeli, A. Mirone, S. L. Chaplot, R. Mittal, E. Ohtani, A. Shatskiy, S. Saxena, S. Ghose, and M. Krisch, *Geophys. Res. Lett.* **43**, 2568 (2016).
- [16] B. Wehinger, A. Bosak, and P. T. Jochym, *Phys. Rev. B* **93**, 014303 (2016).
- [17] B. Wehinger, A. Bosak, G. Piccolboni, K. Refson, D. Chernyshov, A. Ivanov, A. Rumiantsev, and M. Krisch, *J. Phys.: Condens. Matter* **26**, 115401 (2014).
- [18] B. Wehinger, A. Bosak, A. Chumakov, A. Mirone, B. Winkler, L. Dubrovinsky, N. Dubrovinskaia, V. Brazhkin, T. Dyuzheva, and M. Krisch, *J. Phys.: Condens. Matter* **25**, 275401 (2013).
- [19] P. Hohenberg and W. Kohn, *Phys. Rev.* **136**, B864 (1964).
- [20] S. J. Clark, M. D. Segall, C. J. Pickard, P. J. Hasnip, M. I. J. Probert, K. Refson, and M. C. Payne, *Z. Kristallgr. Cryst. Mater.* **220**, 567 (2009).
- [21] H. J. Monkhorst and J. D. Pack, *Phys. Rev. B* **13**, 5188 (1976).
- [22] R. A. Cowley, *Phys. Rev.* **134**, A981 (1964).
- [23] A. Bussmann-Holder, *Phys. Rev. B* **56**, 10762 (1997).
- [24] J. D. Axe, J. Harada, and G. Shirane, *Phys. Rev. B* **1**, 1227 (1970).
- [25] J. Hlinka, M. Quilichini, R. Currat, and J. F. Legrand, *J. Phys.: Condens. Matter* **8**, 8207 (1996).
- [26] A. Kohutych, R. Yevych, S. Perechinskii, V. Samulionis, J. Banys, and Y. Vysochanskii, *Phys. Rev. B* **82**, 054101 (2010).
- [27] A. Bussmann-Holder, H. Büttner, and A. R. Bishop, *Phys. Rev. Lett.* **99**, 167603 (2007).
- [28] A. K. Tagantsev, K. Vaideeswaran, S. B. Vakhrushev, A. V. Filimonov, R. G. Burkovsky, A. Shaganov, D. Andronikova, A. I. Rudskoy, A. Q. R. Baron, H. Uchiyama, D. Chernyshov, A. Bosak, Z. Ujma, K. Roleder, A. Majchrowski, J.-H. Ko, and N. Setter, *Nat. Commun.* **4**, 2229 (2013).
- [29] A. N. Morozovska, M. D. Glinchuk, E. A. Eliseev, and Y. M. Vysochanskii, *Phys. Rev. B* **96**, 094111 (2017).
- [30] S. K. Satija, S. M. Shapiro, M. B. Salamon, and C. M. Wayman, *Phys. Rev. B* **29**, 6031 (1984).
- [31] M. S. Pavlovskiy, K. A. Shaykhutdinov, L. S. Wu, G. Ehlers, V. L. Temerov, I. A. Gudim, A. S. Shinkorenko, and A. Podlesnyak, *Phys. Rev. B* **97**, 054313 (2018).